

Strain Engineering in Monolayer WS₂ and WS₂ Nanocomposites

Fang Wang^{1,2}, Suhao Li¹, Mark A. Bissett¹, Ian A. Kinloch¹, Zheling Li^{1*} and Robert J. Young^{1*}

¹Department of Materials and National Graphene Institute, University of Manchester, Manchester M13 9PL, UK

²Present address: MOE Key Laboratory of Macromolecular Synthesis and Functionalization, Department of Polymer Science and Engineering, Key Laboratory of Adsorption and Separation Materials & Technologies of Zhejiang Province, Zhejiang University, 38 Zheda Road, Hangzhou, 310027, PR China

*E-mail: zheling.li@manchester.ac.uk; robert.young@manchester.ac.uk

Received xxxxxx

Accepted for publication xxxxxx

Published xxxxxx

Abstract

There has been a massive growth in the study of transition metal dichalcogenides (TMDs) over the past decade, based upon their interesting and unusual electronic, optical and mechanical properties, such as tuneable and strain-dependent bandgaps. Tungsten disulfide (WS₂), as a typical example of TMDs, has considerable potential in applications such as strain engineered devices and the next generation multifunctional polymer nanocomposites. However, controlling the strain, or more practically, monitoring the strain in WS₂ and the associated micromechanics have not been so well studied. Both photoluminescence spectroscopy (PL) and Raman spectroscopy have been proved to be effective but PL cannot be employed to characterise multilayer TMDs while it is difficult for Raman spectroscopy to reveal the band structure. In this present study, photoluminescence and Raman spectroscopy have been combined to monitor the strain distribution and stress transfer of monolayer WS₂ on a flexible polymer substrate and in polymer nanocomposites. It is demonstrated that WS₂ still follows continuum mechanics on the microscale and that strain generates a non-uniform bandgap distribution even in a single WS₂ flake through a simple strain engineering. It is shown that these flakes could be useful in optoelectronic applications as they become micron-sized PL emitters with a band gap that can be tuned by the application of external strain to the substrate. The analysis of strain distributions using Raman spectroscopy is further extended to thin-film few-layer WS₂ polymer nanocomposites where it is demonstrated that the stress can be transferred effectively to WS₂ flakes. The relationship between the mechanical behaviour of single monolayer WS₂ flakes and that of few-layer flakes in bulk composites is investigated.

Keywords: micromechanics, electromechanics, transition metal dichalcogenide, photoluminescence, Raman spectroscopy

1. Introduction

The past two decades have witnessed an increasing interest in the application of 2D materials in various applications ranging from device fabrication to polymer composites. As one of the first 2D materials to be isolated graphene, in particular, has been studied extensively [1]. Graphene is, however, an electrical conductor that limits its wider applications where a bandgap is needed. Hence, TMDs have started to attract attention since their tunable bandgap offers more controllability [2, 3]. As a typical example of TMDs, tungsten disulfide (WS_2) has received significant interest for applications in transistors [4], photo-detectors [5], photovoltaic devices [6] and composites [7]. Of particular interest is that WS_2 exhibits a transition from a direct- to indirect-bandgap semiconductor both as the number of layers increases [8] and when the WS_2 flakes are subjected to strain [9]. Beyond the electronic applications, WS_2 flakes have also been found to have a reasonable interfacial interaction with polymers as reflected by their good reinforcement of polymers, determined by their lateral size and its distribution [10], even at a low loadings [10, 11]. This sets the foundation for making use of WS_2 for the next generation multifunctional nanocomposites for a number of different applications, such as transistors, sensors, photo-detectors, photovoltaics and absorbers etc. [4-6, 12].

In spite of the extensive work on the applications of WS_2 , however, relatively little is known about one fundamental core aspect of their behaviour – the deformation micromechanics of WS_2 flakes for strain engineering in nanocomposites. For example, although the Young's modulus of WS_2 has been measured by Liu *et al.* [13] to be ~ 270 GPa, its bilayer exhibits a lower stiffness indicating 25% reduction of stress transfer from one layer to the other due to weak interlayer interaction, similar to that observed in few-layer graphene [14]. The state of strain at the interface between TMDs and polymers, used either as coating in devices or as matrices in thin film composites [15], is also crucial. This is because it is a fundamental aspect of deformation mechanics to ensure that no mechanical failure occurs as well as the core aspect of bandgap control. This highlights the importance of strain engineering, particularly in the monitoring of the local strain in WS_2 flakes and the state of stress at the interface.

Similar to earlier studies upon graphene and graphene oxide [16, 17], Raman spectroscopy has been used to follow the deformation of WS_2 and its Raman bands have been found to undergo a red-shift under tensile strain. In particular, the band widths and intensities are also found to correlate with the level of applied strain [18]. It is difficult, however, for Raman spectroscopy to be used to study the bandgap structure of WS_2 . Instead, photoluminescence (PL) has recently been employed for this purpose in TMDs and it has been found the PL peaks can be used to reveal the structural non-uniformity caused by

strain and doping of MoS_2 , for which the energies of the PL peaks undergo a red shift with tensile strain [9, 19, 20]. This phenomenon was then applied to flexible WS_2 devices to monitor structural uniformity and strain relaxation during cyclic loading [21]. This behaviour is advantageous as PL simultaneously senses the strain as well as monitoring the bandgap in WS_2 , suggesting a method of varying the bandgap in a single WS_2 flake by simple strain engineering. A recent study [22] has shown that it is possible to tailor the PL of TMD monolayers by forming hydrocarbon-filled bubbles of monolayer TMDs on a substrate. These bubbles localise the PL by producing micrometre-sized strain gradients which form so-called "artificial atoms" that are well separated on the substrate. A downside of the PL approach, however, is also apparent since, unlike in Raman spectroscopy, the intensity of PL peaks decreases greatly as the number of layers increases so that most of the PL studies to date have so far concentrated mainly on TMD monolayers [23].

In the present study, we have combined Raman and photoluminescence spectroscopy to monitor the strain distribution in mechanically-cleaved monolayer WS_2 flakes deformed on flexible substrates. This methodology is further extended to WS_2 /poly(vinyl alcohol) nanocomposites where the deformation micromechanics of multilayer WS_2 flakes within the polymer is revealed.

2. Experimental

2.1 Materials and processing

2.1.1 Substrate preparation. A poly(methyl methacrylate) (PMMA) beam was coated by spin coating a 600 nm layer of SU-8 (MicroChem SU-8 2000 Permanent Epoxy Negative Photoresist) as substrate in order to enhance the contrast with the substrate under the optical microscope. The coating was undertaken using a spin coater (WS-650Mz-23NPPB spin coater Laurell Technologies Corporation). The static coating procedure involved dispensing 0.5 ml of the SU-8 resin on the PMMA substrate, followed by 10 s spinning at 500 rpm with 100 rpm/s acceleration and 30 s at 2000 rpm with 300 rpm/s acceleration [24]. The specimens were then subjected to a 1 min soft bake at 95 °C and 2 min post bake at 95 °C [24].

2.1.2 Exfoliation and transfer. Monolayer WS_2 flakes were obtained by the exfoliation through the micromechanical cleavage [25] of bulk WS_2 crystals with an average grain size of 200 μm supplied by HQ Graphene, Groningen, the Netherlands. The bulk WS_2 crystals were peeled repeatedly with an adhesive tape until very thin flakes were obtained.

The flakes obtained were then transferred to the PMMA substrate with a lay of SU-8 on top by pressing the back of the adhesive film. After the transfer, monolayer flakes were located and identified using optical microscopy and a

combination of Raman and photoluminescence (PL) spectroscopy.

2.1.3 Nanocomposite preparation. Liquid-phase exfoliation was employed to produce WS₂ dispersions, termed LPE WS₂. A detailed procedure of the exfoliation was reported earlier by Bissett *et al.* [26]. Briefly, dispersions of LPE WS₂ were produced by ultrasonication for 12 hours of commercially-available WS₂ powder (Sigma-Aldrich) in a mixture of isopropanol and water (1:1 v/v) at a concentration of 10 mg/ml [26]. This was followed by centrifugation at three different speeds (1500, 3000 and 6000 rpm) so that a range of lateral dimensions could be obtained, namely LPE WS₂-L, LPE WS₂-M and LPE WS₂-S, respectively. The WS₂/PVA thin film nanocomposites were fabricated *via* a solution-mixing method. The poly(vinyl alcohol) (PVA, Sigma-Aldrich) was firstly dissolved in deionized water at ~90 °C to form aqueous solutions (~50 mg/ml). The polymer solutions were mixed with the dispersions of WS₂ in the appropriate ratio with WS₂ to give loadings of 0.5, 0.8, 1.2, 2.0 and 5.0 wt%, respectively, followed by a short sonication (~5 min). Finally, the solutions were dried at room temperature for a few days (> 48 h) to obtain the composites. The LPE WS₂ loading was converted to volume fraction V_f (vol%) from the weight fraction W_f (wt%) using the following equation:

$$V_f = \frac{W_f \rho_p}{W_f \rho_p + (1 - W_f) \rho_w} \quad (1)$$

where ρ_p and ρ_w are density of the polymer and WS₂ flakes, which were taken as 1.3 g/cm³ [17] and 7.5 g/cm³ [27], respectively. As a result, the 0.5, 0.8, 1.2, 2.0 and 5.0 wt% weight fraction loadings are converted to volume fractions of 0.09, 0.14, 0.21, 0.35 and 0.90 vol%, respectively.

2.2 Characterisation

An atomic force microscope (AFM, Bruker dimension 3100) was used in the tapping mode to provide morphological information about the WS₂ flakes deposited onto a Si/SiO₂ substrate. For transmission electron microscopy (TEM) analysis, the WS₂ flakes were tape exfoliated onto a Si/SiO₂ substrate. They were then transferred to a lacey-carbon Cu TEM grid via a polymer-free technique. The TEM phase contrast images were obtained using A JEOL 2100 field emission TEM with an accelerating voltage of 200 kV in a bright field detector. The acquisition time was between 0.5 s and 2.5 s.

The concentrations of WS₂ dispersions were determined using a UV-Visible spectrophotometer (Thermal Scientific Evolution 201) with a Beer's Law Coefficient of 2756 ml/mg/m (for peak at $\lambda=629$ nm) [28]. Raman and PL spectroscopy were conducted using a Horiba LabRam system using $\lambda=488$ nm laser excitation at room temperature. The

laser power for both spectroscopy measurements was set at a low level to avoid laser heating of specimens. The orientation of the LPE WS₂ filler was examined using polarised Raman spectroscopy [29]. The *in-situ* deformation testing of the LPE WS₂/PVA nanocomposites was undertaken using a Renishaw system 1000 Raman spectrometer with a $\lambda=514.5$ nm laser excitation with low power (<0.2 mW). The tensile properties of the neat PVA and LPE WS₂/PVA composites with different WS₂ loadings were determined based on the ASTM D3039 method using an Instron-1122 universal testing machine. Prior to mechanical testing, the specimens were left for 24h in an air-conditioned laboratory where the temperature was set as 23.0 ± 0.1 °C with a relative humidity of $\sim 50 \pm 5\%$. The specimens were deformed using a crosshead speed of 1 mm/min and four or five specimens for the neat PVA sample and each of the LPE WS₂/PVA composites sample were tested.

2.3 In-situ deformation with PL and Raman spectroscopy

For deformation of the monolayer WS₂ flakes, the PMMA substrate was mounted on a 4-point bending rig and placed under the microscope stage in Raman spectrometer. A resistance strain gauge was fixed to the PMMA beam close to the WS₂ flakes to monitor the strain. The specimen was then deformed stepwise with the Raman or PL spectra collected for each strain step. Mapping was undertaken using a grid size of $0.5 \mu\text{m} \times 0.5 \mu\text{m}$ or $1 \mu\text{m} \times 1 \mu\text{m}$ depending upon sizes of the flakes and the degree of precision needed. The laser was polarised parallel to the direction of tensile strain. For the deformation test of thin film nanocomposites, the films were mounted and stretched in a tensile rig designed in house and Raman spectra were obtained for the LPE WS₂/PVA nanocomposites. The details of the experimental method have been described in detail in our previous report [7].

3. Results and Discussion

3.1 Photoluminescence spectroscopy of monolayer WS₂

Figure 1a shows an optical image of a typical WS₂ flake prepared *via* micromechanical cleavage consisting of a thick multilayer and a monolayer adjacent to it as confirmed by PL. Figure 1b shows the PL spectrum of the monolayer consisting of an extremely strong peak with two features, namely: a dominant peak centered at ~2.00 eV corresponding to a neutral A exciton and a weaker peak with slightly lower energy known as the Trion exciton (A⁻ exciton) caused by undesired doping during exfoliation [30, 31]. In contrast, Figure 1c also shows that the intensity of the PL peaks reduces significantly as the number of layers of WS₂ increases, and the spectrum from the bulk crystal shows nearly no peak at all [23, 32]. This is a result of the WS₂ undergoing the transition from indirect band

gap (Γ -K) to direct band gap (K-K) semiconductor as the number of layer decreases towards monolayer [23, 32]. This can therefore be used to identify monolayer WS_2 since only the monolayer region shows a strong intensity of the A exciton peak whereas there is no detectable signal from thicker counterparts (inset in Figure 1a).

The high sensitivity of PL spectroscopy to detect features at the submicron level also reveals some non-uniformity around the centre of flake where wrinkles and contaminant are present [20]. This can also be seen by the AFM (Figure 1d)

The AFM height profile also shows some contamination on the flake, perhaps due to bubbles trapped by the flake, commonly seen for micromechanically-exfoliated flakes of 2D materials [22, 33]. It should be noted that the height profile along the line in Figure 1d is around 10 nm, significantly greater than the thickness of WS_2 monolayer. This may arise from high degree of roughness and viscoelastic nature of polymer substrate. The lattice structure of the WS_2 flakes can also be clearly seen by using atomic resolution TEM as shown in Figure 1e [7].

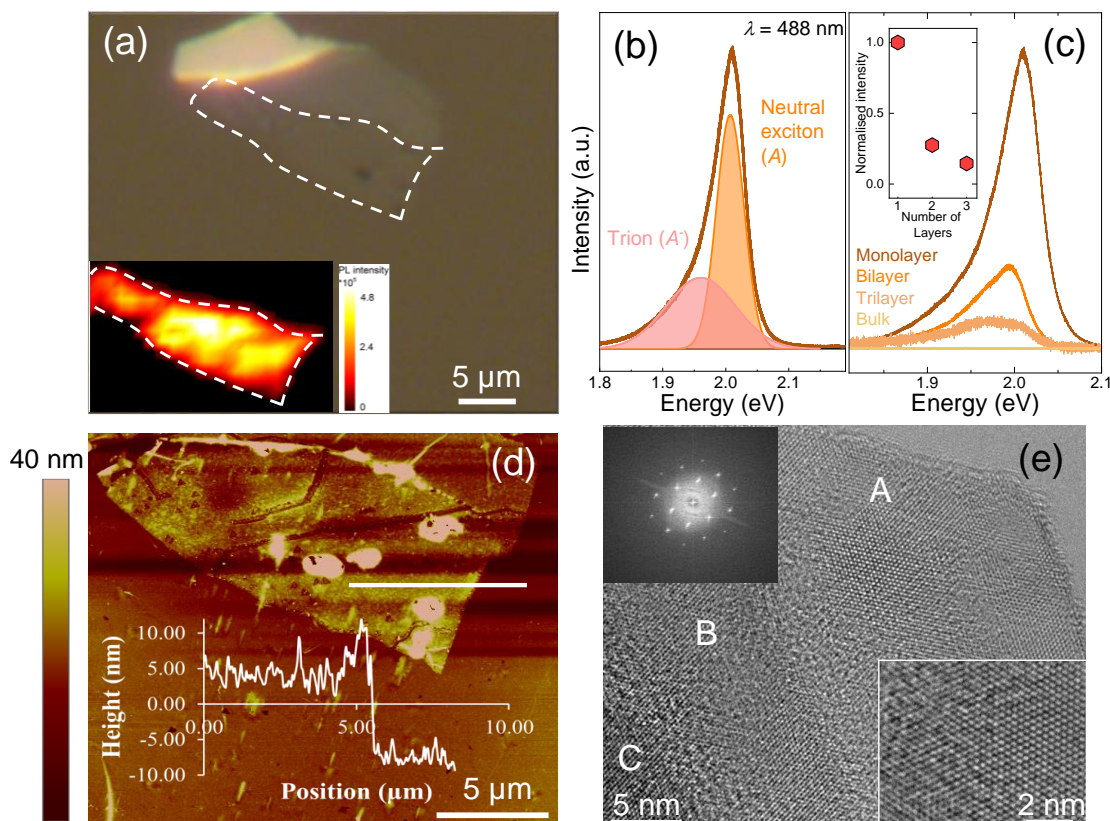


Figure 1. (a) Optical image of a monolayer WS_2 flake (outlined) along with a multilayer flake. The inset in (a) is the PL intensity mapping of the A exciton peak which only highlights the monolayer flake. (b) PL spectrum of the monolayer WS_2 flake in (a). (c) The PL spectra of WS_2 flakes with different numbers of layers. The inset shows their normalised intensity. (d) AFM micrograph of the monolayer flake in (a). The height profile along the white line in (d) is shown as inset. (e) TEM image of a WS_2 flake with regions of different thickness. Areas A, B, and C show the atomic structure most likely of single, double, and triple layers, respectively. The lower inset clearly indicates an atomically clean WS_2 lattice, and the FFT image in the top inset indicates the crystalline nature of the flake. (Image courtesy of Eoghan O'Connell and Ursel Bangert, University of Limerick, Ireland)

Figure 2a is the schematic diagram the PMMA substrate with SU-8 top coating in the 4-point bending rig placed on the stage of the Raman spectrometer [16, 34]. It should be noted that the size of WS_2 flake ($\sim 10 \mu\text{m}$) is three orders of magnitude smaller than the length of substrate ($\sim 70 \text{mm}$) so that the flake can be assumed to be strained uniaxially [16]. A

clear red-shift of the PL peak can be seen as the strain level increases, with the peak fitted with two Gaussian peaks (Figure 2b) [7, 35]. Since the band gap in monolayer WS_2 is mostly determined by the 3p orbital of the S atoms and the 5d orbital of the W atoms [36, 37], the red-shift occurs as the strain alters the W-W and W-S bond lengths, giving rise to a

reduction in the orbital hybridization and d-band width [38]. In more detail, as the strain increases, the red-shift of both the A exciton peak and A^- exciton peak is in the order of tens of meV as shown in Figure 2c, which agrees with other studies on TMDs [19, 23, 38, 39]. The shift rate is found to be -58.7 ± 1.4 meV/% strain for the A exciton peak, and -89.9 ± 4.9 meV/% strain for the A^- exciton peak, respectively. The apparent tension at 0% strain is likely to be due to the residual strain induced during specimen preparation. These shift rate values are similar to those predicted by theoretical simulation [40], and amongst the highest experimental values reported [35, 41].

The PL spectra x - y mapped on a $0.5 \times 0.5 \mu\text{m}$ grid across a monolayer WS_2 flake, in a region showing no contamination,

(Figure 2d) were collected at both 0% and 0.35% strain, A reduction of the energy (bandgap) can be clearly seen towards the centre of the flake for 0.35% strain (Figure 2e). This implies that the simple uniaxial tension applied to the monolayer flake on the substrate generates a non-uniform bandgap distribution across an individual WS_2 flake. This is of particular relevance for local fine tuning of the bandgap in a TMD flake through strain engineering [20]. The PL energy varies by some 40 meV over a region of a few microns in the WS_2 monolayer crystals at 0.35% strain. Moreover, this variation of PL energy can be controlled by the application of external strain to the substrate as long as the WS_2 monolayer crystals remain intact and do not debond from the substrate.

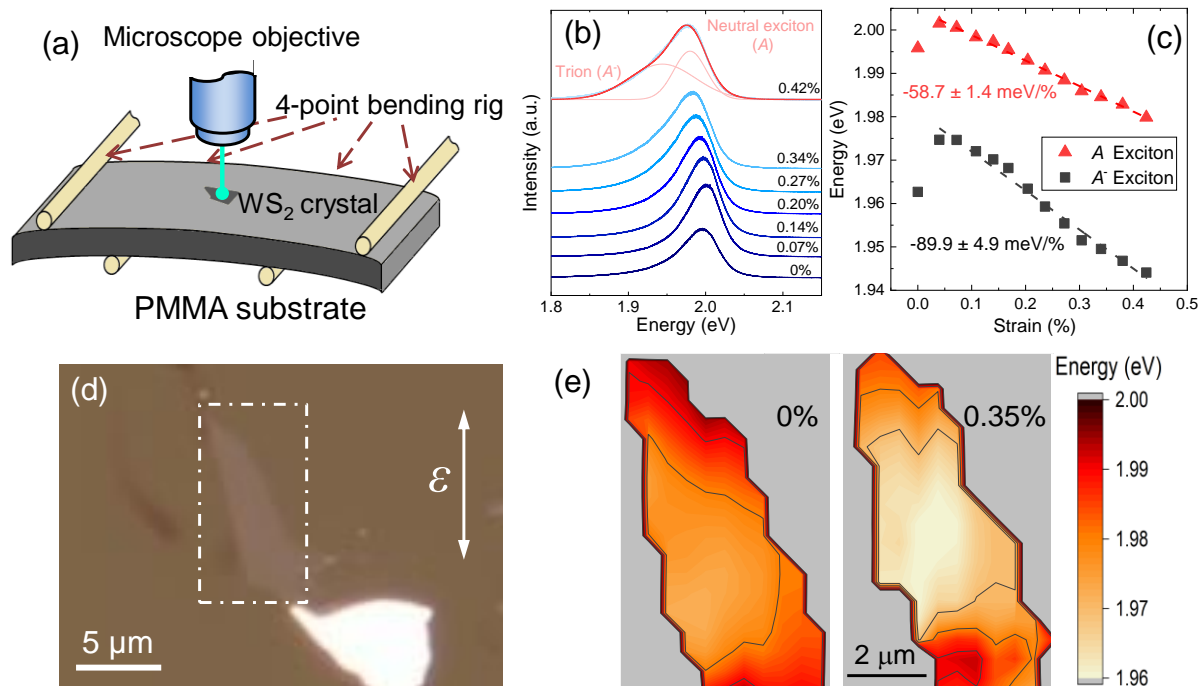


Figure 2. (a) Schematic drawing of the ‘*in-situ*’ deformation set up in PL and Raman spectroscopy. (b) Evolution of the PL spectrum of a monolayer WS_2 flake as strain increases. (c) The energies of A exciton and A^- exciton peaks as a function of strain, with the solid lines being the linear fitting. (d) Optical image of one monolayer WS_2 flake. (e) Map of the A exciton peak energy over the flake at (a) 0% and (b) 0.35% strain.

It is interesting to compare and contrast this present study with that of Tyurina and coworkers [22] who demonstrated that it was possible to tailor the PL using hydrocarbon-filled bubbles under monolayer TMDs on a substrate. Although they were able to localise the PL variation in submicron regions (“artificial atoms”) they were only able to tune the behaviour through the choice of different TMDs rather than by external strain as demonstrated in our study.

The measurements of the positions of the A exciton peaks in Figure 2e were converted to the strain through the use of the correlation found in Figure 2c, leading to maps of the monolayer WS_2 strain distributions at different applied strain

(the strain that was applied to the substrate) levels (Figure 3a & b). It can be seen that at 0% applied strain the flake has an average strain about 0% but with some variation, which could be attributed to the formation of wrinkles in the flake from the specimen preparation by pressing the flake onto the substrate [42, 43], that can be flattened by the tensile strain applied afterwards. When the applied strain is increased to 0.35%, the strain in the flake is found to increase from the edges and eventually plateau in the middle of the flake. This behaviour is shown more clearly in Figure 3c where the variations of strain along the dashed lines shown in Figures 3a & b are plotted.

The behaviour shown in Figure 3 is characteristic of that seen during the deformation of monolayer graphene on a substrate for which it has been demonstrated that continuum mechanics [44] can be employed to model strain distributions using the well-established ‘shear-lag’ theory [16, 45]. In this theory, the strain in the WS₂ flake, ε_f , at a position x along the strain direction is given by an equation of the form [16, 46]:

$$\varepsilon_f = \varepsilon_m \left[1 - \frac{\cosh\left(\frac{nsx}{l}\right)}{\cosh(ns/2)} \right], \quad n = \sqrt{\frac{2G_m}{E_f} \left(\frac{l}{T}\right)} \quad (2)$$

where ε_m is the level of strain applied to the matrix, E_f is the Young’s modulus of the WS₂ flake, G_m is the shear modulus of the polymer, l is the length of WS₂ flake along with strain direction, t and T are the thickness of the WS₂ flake and the representative volume, respectively and s is the aspect ratio of the WS₂ flake (l/t).

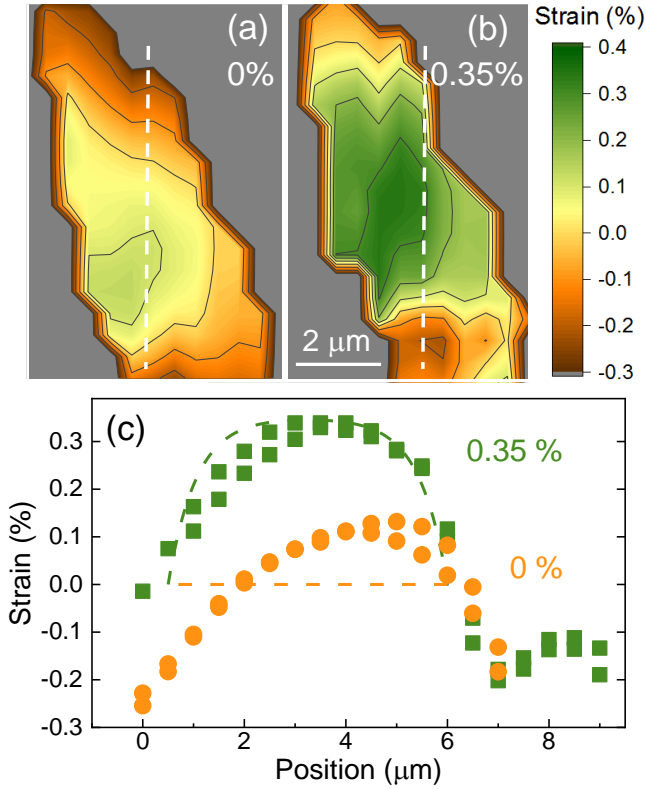


Figure 3. Strain distribution in the monolayer WS₂ flake measured using position of the A exciton peak at (a) 0% and (b) 0.35% applied strain. (c) Extracted strain distribution in the region along the white dashed line (starting from the top) in (a) and (b). The dashed line is indicative of the strain distribution at 0% strain (orange) and 0.35% strain (green) drawn using the shear-lag analysis (Eq. 2) with $ns=10$.

A ‘shear-lag’ curve drawn using Eq. 2 with $ns = 10$ (Figure 3c) at an applied strain $\sim 0.35\%$ shows the shear-lag theory to

be an effective model to predict the behaviour of WS₂ flake on a polymer substrate, and suggests an intact interface between monolayer and polymer. The critical length, l_c , which is defined as twice the distance from the flake edge (0% strain) to where 90% of the maximum strain occurs [46], has also been estimated to be in the order of $\sim 4 \mu\text{m}$ at a strain of 0.35%, which provides an important guideline regarding the minimum lateral dimension of WS₂ flakes reinforcing nanocomposites. Similarly, the variation of the shear stress, τ , along the WS₂ flake can be determined by developing Eq. 2 using a force balance [16] to give:

$$\tau = nE_f\varepsilon_m \frac{\sinh\left(\frac{nsx}{l}\right)}{\cosh(ns/2)} \quad (3)$$

By using $ns = 10$, $E_f = 272 \text{ GPa}$ [13] and $t = 0.65 \text{ nm}$ [13], the shear stress at the edges of the monolayer WS₂ flake is found to be $\sim 1.1 \text{ MPa}$. This value is similar to that found for monolayer graphene [16, 47] but is an order of magnitude lower than that of the carbon fibres in composites ($\sim 20\text{-}40 \text{ MPa}$) [46].

Although found previously for graphene [16], graphene oxide [45] and MoS₂ [20], it is shown previously [44] and in this work that monolayer WS₂ also follows continuum mechanics at the microscale. Hence it seems that this behaviour may be typical for all 2D layered materials. In particular, it has been demonstrated that the non-uniformity of strain determines the distribution of the bandgap, as monitored by the energy of PL peak. This suggests a way of tuning the bandgap of WS₂ even within a single flake by making use of the non-uniformity in strain-engineered TMDs.

A recent study [48] has reviewed the experimentally-determined PL shift rates for a number of TMDs, including WS₂. Values of shift rate ranging from as low as $-1.3 \text{ meV}/\%$ [49] to $-61.8 \pm 3.8 \text{ meV}/\%$ [50] have been reported for the A exciton peak of WS₂. The shear lag analysis described above enables this discrepancy to be explained. The stress transfer efficiency is controlled by the parameter ns and the interaction of the WS₂ flake with the substrate [51]. Better stress transfer is given by high values of ns , i.e. using stiffer substrates (with higher G_m values leading to a higher n) and long flakes with high aspect ratios s . For example the low value of shift rate was found using a very flexible polydimethylsiloxane (PDMS) substrate [49]. This present study used long monolayer flakes on a relatively-stiff PMMA substrate with a layer of SU-8 top coating.

3.2 Raman spectroscopy of WS₂ flakes

As shown above, the intensity of the PL peaks in WS₂ drops significantly as the number of layers increases. This limits its wider application in fields where few-layer and multilayer TMDs are employed, such as in nanocomposites [15]. In contrast, the intensity of the Raman bands in WS₂ tends to increase as the number of layers increases and so Raman

spectroscopy can therefore, be employed both as a complementary technique for strain measurement and for comparison purposes.

Monolayer and few-layer WS₂ flakes were located on a substrate (Figure 4a) and their Raman spectra are shown in Figure 4b. The monolayer was confirmed by the characteristic strong PL emission (inset in Figure 4b) and, in the Raman spectra, the increase of number of layers results in the increasing separation between E_{2g}^1 and A_{1g} bands (~ 62 cm⁻¹ for monolayer) [52]. As the tensile strain is increased up to $\sim 0.55\%$, both the E_{2g}^1 and A_{1g} bands of the monolayer and few-

layer WS₂ not only undergo a detectable red-shift, but also show a splitting of the E_{2g}^1 band into two bands, namely the E_{2g}^{1-} and E_{2g}^{1+} mode, respectively (Figure S1). This arises from the removal of the degeneracy of the E_{2g}^1 mode as a result of strain [35, 39]. As the E_{2g}^{1+} band stays nearly unshifted, we will now demonstrate how the use of the Raman E_{2g}^1 mode in a similar way to our previous report [7] enables the strain in WS₂ flake to be determined. (The band will be referred to as the E_{2g}^1 mode in the following discussion for simplicity).

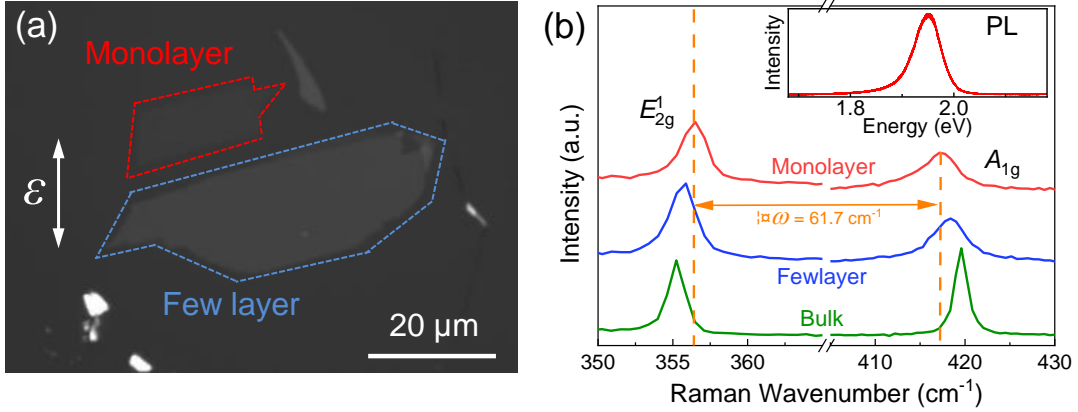


Figure 4. (a) Optical micrograph of monolayer and few layer WS₂ flakes. (b) Raman spectra of monolayer, few-layer and bulk WS₂ flakes. The inset shows the PL spectrum of a monolayer WS₂ flake.

In order to investigate the micromechanics of monolayer WS₂ flake using Raman spectroscopy, the PMMA beam was deformed using the procedure summarised in Figure S2. Briefly, the beam with monolayer WS₂ on top was deformed initially to a strain $\sim 0.55\%$. The specimen was then released and top-coated with a thin layer of SU-8 photoresist polymer. In the second cycle the specimen was then loaded to the same

strain of $\sim 0.55\%$. Using the calibration between the Raman E_{2g}^1 band and strain established in our previous study [7], the strain distributions of the uncoated monolayer WS₂ at 0% and 0.55% applied strain were mapped using a 1 μm × 1 μm grid as shown in Figure 5a and b, respectively.

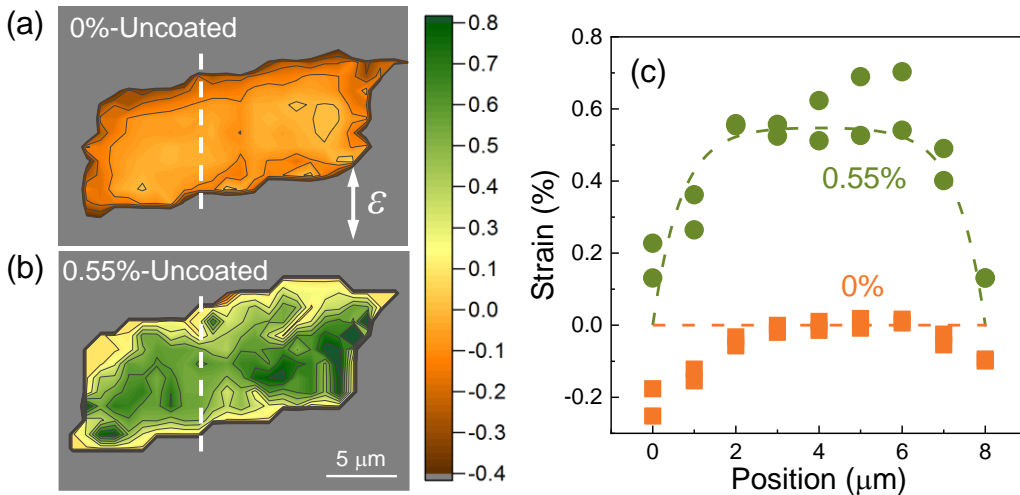


Figure 5. Strain distribution of uncoated monolayer WS₂ flake at (a) 0% and (b) 0.55% applied strain. (c) Extracted strain distribution in the region along the white dashed lines in (a) and (b) determined from the frequency of E_{2g}^1 mode. The dashed lines are indicative of strain distribution at 0% and 0.55% strain drawn using the shear-lag analysis Eq. 2 with $ns=12$.

It can be seen that the strain distribution in Figure 5 is quite uniform at 0% strain, apart from the compression at the edge of flake perhaps due to sample preparation. The similarity between the strain distributions shown in Figure 5 obtained using Raman spectroscopy and those obtained for a similar WS₂ monolayer specimen using PL in Figure 3 is striking.

When the specimen was subjected to a strain of 0.55%, the strain in most of the WS₂ flake increased to about 0.55%, demonstrating effective stress transfer from the substrate to the flake. However, a slight strain concentration, higher than the applied strain $\sim 0.55\%$, can be found in the bottom part perhaps due to defects or edge effects [53]. The data points extracted along the vertical dashed white lines in tensile strain direction (Figure 5c) clearly show a strain plateau in the middle of the flake at the strain of 0.55%, suggesting that monolayer WS₂ flake also follows the shear lag behaviour shown in Figure 3. Similarly, by using $ns = 12$ in Eq. 2, the ‘shear-lag’ curve is drawn for an applied strain $\sim 0.55\%$ (Figure 5c). Similar to the behaviour shown in Figure 3d, the curve matches the data points very well, further confirming the validity of shear-lag theory. The shear stress at the edges of the monolayer WS₂ flake is found to be ~ 1.5 MPa (Eq.3), similar to that found by using PL (Figure 3).

The specimen shown in Figure 5 was unloaded and a top coat of SU-8 applied so that the deformation of the WS₂ monolayer sandwiched between two polymer films, as in a nanocomposite, could be studied as shown in Figure 6. Although the strain in the monolayer is relatively uniformly distributed at 0% strain (Figure 6a) it is, however, reduced to $\sim -0.35\%$ which means that there is a uniform 0.35%

compressive strain in the flake as a result of the shrinkage of the top-coating SU-8 polymer during curing [54]. Subsequently, the coated flake was subjected to a strain of 0.55% (Figure 6b) and a strain concentration at top part of the flake is observed. The ‘shear-lag’ curve drawn using Eq. 2 ($ns=12$) for an applied tensile strain of 0.55% is offset by -0.35% to take into account the 0.35% compressive strain, hence the maximum strain is only about 0.20% [53]. In addition the strain drops sharply in the middle of the flake although the strain distribution of other parts still approximately follows the shear lag curve (Figure 6c). The reason for this is attributed to the occurrence of two cracks in the middle of the WS₂ flake perpendicular to the tensile axis as highlighted with dashed white frames and the inset in Figure 6b, similar to the fracture behaviour observed for monolayer graphene [55]. This implies that the failure strain of this WS₂ flake is no more than 0.55%, due probably to the presence of defects. This strain to failure, in combination with its Young’s modulus ~ 272 GPa [13], implies the strength of this monolayer WS₂ flake was ~ 1.5 GPa. The interfacial adhesion has not been improved by the SU-8 top coating. This is because for monolayer WS₂ sandwiched and stretched between SU-8 layers, the adhesion with one side interface is not significantly different from that with double sides. This is in similarity with graphene, but if few-layer graphene is stretched the SU-8 top coating can provide extra adhesion to compensate for the interlayer sliding due to the weak interlayer bonding [14].

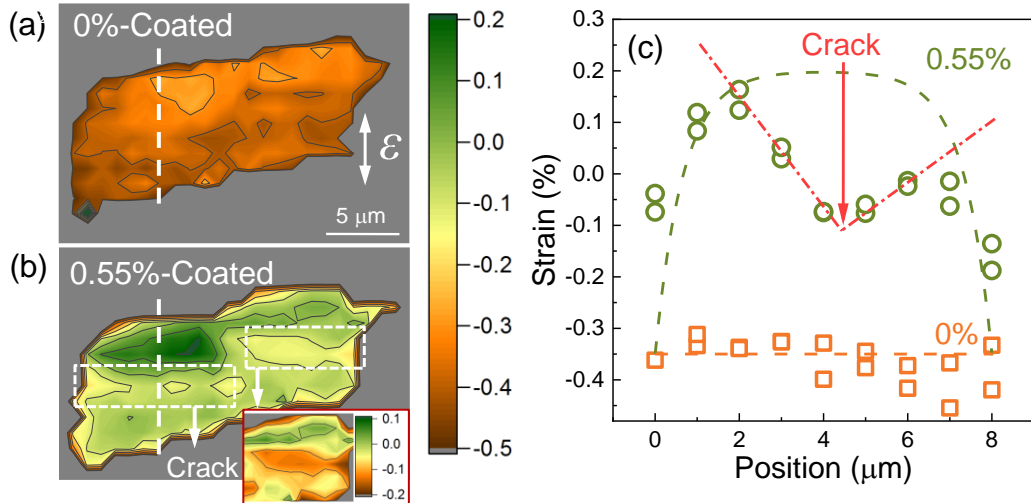


Figure 6. Strain distribution of coated monolayer WS₂ flake at (a) 0% and (b) 0.55% applied strain. In (b) the location of crack is also indicated. The right crack is highlighted as the inset with a finer strain scale. (c) Extracted strain distribution in the region along the white dashed lines in (a) and (b) determined from the Raman frequency of E_{2g}^{1-} mode. The dashed lines are indicative of strain distribution at 0% and 0.55% strain drawn using the shear-lag analysis in Eq. 2 with $ns=12$.

3.3 Thin film WS₂/PVA nanocomposites

We extended our analysis of the deformation micromechanics of monolayer WS₂ further to that of bulk few-layer WS₂/PVA nanocomposites. The few-layer WS₂ flakes were liquid-phase exfoliated in large quantities and separated by centrifugation into three grades based on their lateral dimensions, namely, large (LPE WS₂-L), medium (LPE WS₂-M) and small (LPE WS₂-S) WS₂ flakes [56]. The lateral size distributions of each grade, measured from SEM images for more than 60 flakes of each grade, are presented in Figure 7a. It can be seen that LPE WS₂-L, LPE WS₂-M and LPE WS₂-S have average lateral sizes of $8.1 \pm 4.7 \mu\text{m}$, $2.4 \pm 2.1 \mu\text{m}$ and $1.0 \pm 0.5 \mu\text{m}$, respectively.

Raman spectra of the LPE-WS₂ flakes, neat PVA and their nanocomposites are shown in Figure 7b, with both the E_{2g}^1 and A_{1g} bands can be clearly identified in the nanocomposites. The position of the E_{2g}^1 band ($\omega(E_{2g}^1)$) was used to monitor the strain in the WS₂ flakes during deformation of the nanocomposites containing the few-layer WS₂ flakes of different lateral dimensions. It can be seen in Figure 7c that the nanocomposites reinforced with LPE WS₂-L flakes exhibit a significant red-shift at a rate of $-0.66 \pm 0.15 \text{ cm}^{-1}/\%$ strain (Raman spectra shown in Figure S3), while the shift rate

decreases as the lateral dimension decreases because of lower level of reinforcement provided by the smaller flakes [34]. It was found that the rate of band shift decreased WS₂-L/PVA above $\sim 0.3\%$ strain due possible to failure of the interface between the PVA and WS₂ flakes above this strain [57]. This is further evidenced by similar behaviour of the A_{1g} band (Figure S4) where the LPE WS₂-L flakes show significantly larger shift than the other two. The results were found to be very reproducible, in that only the LPE WS₂-L flakes with large lateral dimensions of $8.1 \pm 4.7 \mu\text{m}$ give rise to good stress transfer and so can be used to reinforce nanocomposites effectively.

The critical length for the monolayer WS₂ flakes was found to be $\sim 4 \mu\text{m}$ and this is indicated on Figure 7a. It should be noted that the lateral sizes of most of the LPE WS₂-L flakes are higher than $4 \mu\text{m}$ whereas they are lower than $4 \mu\text{m}$ for the LPE WS₂-M and LPE WS₂-S flakes. This is clear indication of the importance of flake size in having good stress transfer in nanocomposites [58]. It is likely that the larger flakes may also be thicker and it might be better to consider the flake aspect ratios, s , rather than just their lateral dimensions for a complete analysis in the future.

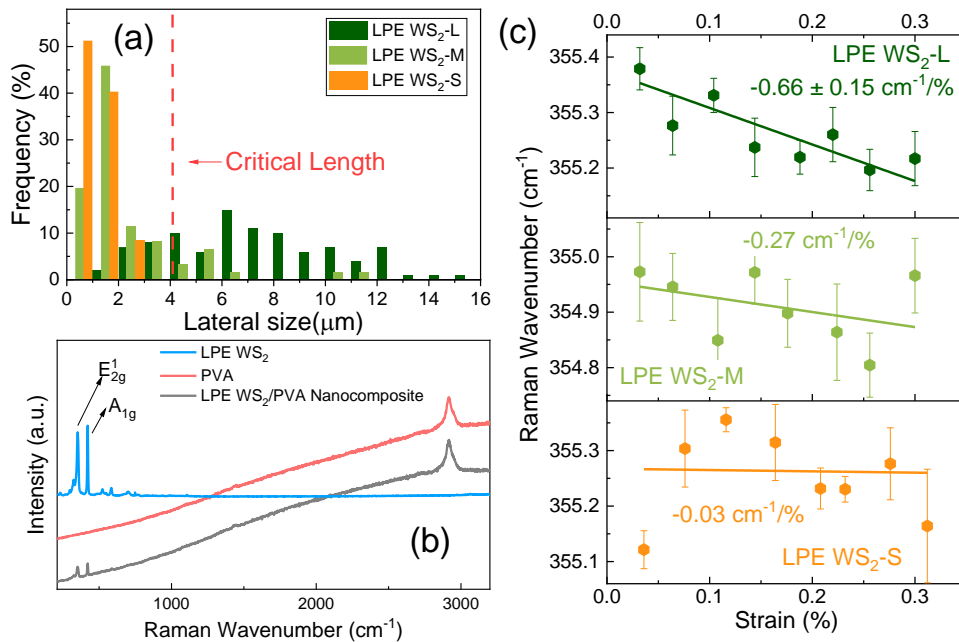


Figure 7. (a) Distribution of lateral size of the LPE WS₂-L, LPE WS₂-M and LPE WS₂-S flakes. (b) Raman spectra of the LPE WS₂ flakes, neat PVA and their nanocomposites. (c) Shift of Raman E_{2g}^1 band as the function of strain of nanocomposites reinforced by LPE WS₂-L, LPE WS₂-M and LPE WS₂-S, respectively. The straight lines are the linear fit of the corresponding data points.

The Raman band shift rate reveals the level of strain in the materials as a result of stress transfer from matrix and the stress/strain-induced Raman band shift and has been used to

estimate the effective modulus of graphene [59], graphene oxide [17] and boron nitride [60] in nanocomposites. We have

made an attempt to extend this methodology to WS₂ flakes [45]. The effective modulus of the reinforcement is given by

$$E_{\text{eff}} = \frac{d\omega(E_{2g}^1)}{d\varepsilon} \cdot \frac{E_f}{d\omega(E_{2g}^1)/d\varepsilon(\text{ref})} \quad (4)$$

where $d\omega(E_{2g}^1)/d\varepsilon$ is the shift rate of the Raman E_{2g}^1 band as the function of strain ε . The reference band shift rate value, $d\omega(E_{2g}^1)/d\varepsilon(\text{ref})$ for the deformation of isolated flakes can be taken as $-2.05 \text{ cm}^{-1}/\%$ as found previously [7]. If the Young's modulus of a monolayer WS₂ flake E_f is taken as 272 GPa [13], then the value of $d\omega(E_{2g}^1)/d\varepsilon$ measured $-0.66 \pm 0.15 \text{ cm}^{-1}/\%$ for LPE WS₂-L flakes in this work (Figure 7c) leads to an effective modulus of LPE WS₂-L (E_{eff}) of $\sim 87 \pm 20 \text{ GPa}$, i.e. around 30% of the value of 272 GPa determined from the direct measurement on monolayer flakes [13]. No apparent slipping in either model devices or nanocomposites has been observed in PL and Raman experiments. This is for two reasons: (1) the level of strain achieved is not sufficiently high

to induce an interfacial damage and (2) the WS₂ flake cracks first prior to the interfacial failure, probably due to the fact that the strength of WS₂ is not as high as graphene, especially with the presence of defects [55].

We also investigated the reinforcement of the WS₂/PVA nanocomposites further by undertaking tensile testing upon the nanocomposites reinforced with different loadings of the LPE WS₂-L flakes. The stress-strain curves in Figure 8a show that the incorporation of WS₂ at low loadings (up to $\sim 0.21 \text{ vol}\%$) there is a linear increase in the Young's modulus of the nanocomposites (E_c) (Figure 8). Above this loading, the reinforcement efficiency from the WS₂ decreases, probably due to aggregation and percolation effects [61], although the maximum E_c is found to be $\sim 940 \pm 38 \text{ MPa}$ for the highest loading, corresponding to nearly a 60% increase in modulus with respect to the neat PVA. In contrast, the strain to failure and ultimate strength remain unchanged, regardless of the WS₂ loading (Figure 8a). These findings are consistent with the Raman band shifts shown in Figure 7c.

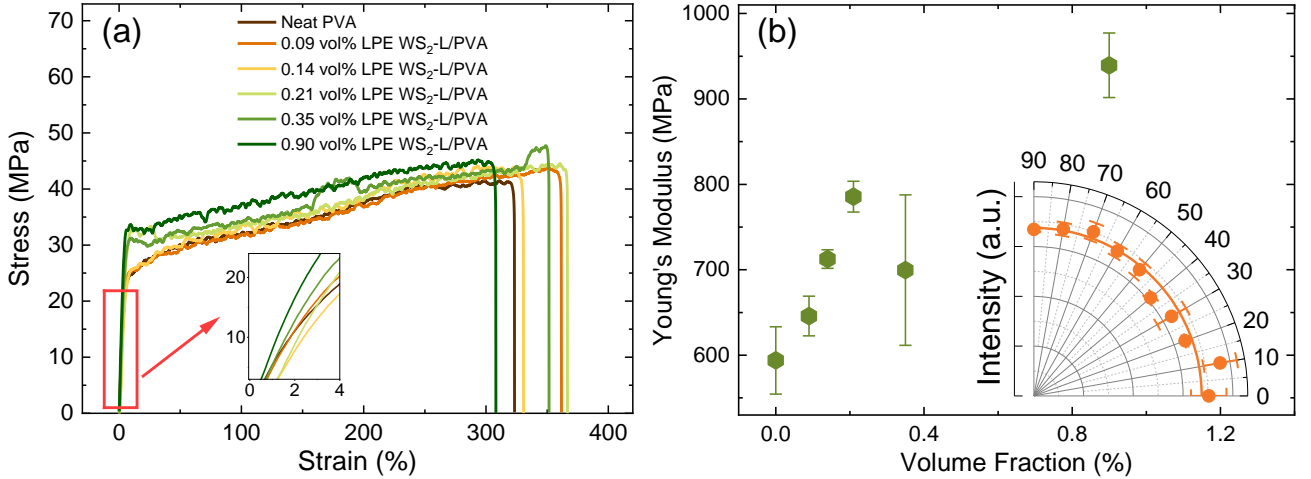


Figure 8. (a) Stress-strain curves for the neat PVA and LPE WS₂-L/PVA nanocomposites with different LPE WS₂-L flake loadings. (b) Young's modulus of the neat PVA and nanocomposites with different LPE WS₂-L loadings. The inset is the intensity of Raman A_{1g} band as the function of rotation angle.

We have demonstrated previously that the Young's modulus of the nanocomposites, E_c , can be analysed using the modified rule of mixtures [46, 58]:

$$E_c = E_{\text{eff}}V_f + E_m(1-V_f) \quad (5)$$

where E_{eff} is the effective Young's modulus of LPE-WS₂, E_f and E_m are the Young's modulus of the LPE-WS₂ and PVA, respectively. V_f is the volume fraction of WS₂ in the nanocomposites. Figure 8b shows a linear increase of E_c as the function of V_f , up to 0.21 vol% loading that enables the E_{eff} to be determined as $\sim 93 \text{ GPa}$, similar to that obtained from

Raman band shifts using Eq. 4, validating the use of Raman spectroscopy to predict the value of E_{eff} for the TMDs.

The effective modulus of WS₂ flakes in the nanocomposites is given by [58]

$$E_{\text{eff}} = \eta_l \eta_o E_f \quad (6)$$

The length factor, η_l , which has a value of between 0 and 1, reflects the dependence of reinforcement on flake length and increases with the flake aspect ratio s [62]. The Krenchel orientation factor η_o enables the effect of filler orientation upon the reinforcement efficiency to be determined and it ranges from 8/15 for randomly oriented to 1 for well-aligned

flakes [29, 63]. Polarised Raman spectroscopy (inset in Figure 8b) shows that the intensity of the A_{1g} band is independent of the angle of direction of laser polarisation. This corresponds to a random orientation of the WS_2 flakes in the nanocomposites, based on the methodology established earlier [29]. The length factor η_l is given by [64]

$$\eta_l = 1 - \frac{\tanh(ns/2)}{ns/2} \quad (7)$$

The parameter ns was found to be of the order of 10 for the monolayer flakes which would give value of $\eta_l \sim 0.8$ (Eqs. 2 and 7) as the average number of WS_2 layers is about 1-3 [26]. Considering the above, the values of E_f can be calculated to be up to 220 GPa according to Eq. 6, in broad agreement with the experimental theoretical value ~ 270 GPa. It should be noted that the value of E_f may also be lower for few-layer materials than the monolayer, as has been found for graphene [14], due to interlayer sliding.

4. Conclusions

In this work, photoluminescence and Raman spectroscopy have been combined to successfully monitor the strain distribution and stress transfer of monolayer WS_2 on a flexible polymer substrate and also in thin film bulk nanocomposites. It is demonstrated that monolayer WS_2 still follows continuum mechanics. Particularly, a non-uniform bandgap distribution has been achieved by strain engineering even within a single WS_2 flake due to the non-uniform strain distribution through stress transfer from the substrate. It has been demonstrated that this could have useful applications in optoelectronics in producing tuneable micron-sized PL emitters on a substrate. The micromechanics developed for monolayer WS_2 flake has been extended to thin film nanocomposites, where it has been found that the stress can be transferred effectively to thicker WS_2 flakes. Their effective Young's modulus is around 30 % of their theoretical modulus which means that their reinforcement efficiency is comparable to that of few-layer graphene-reinforced nanocomposites.

Acknowledgements

This research has been supported by funding from the European Union Seventh Framework Programme under grant agreement n°604391 Graphene Flagship and the EPSRC (award no. EP/I023879/1). The authors are grateful to Eoghan O'Connell and Ursel Bangert, Bernal Institute, Department of Physics and Energy, University of Limerick, Limerick, Ireland, for help with the TEM analysis.

References

1. Kong W, Kum H, Bae S-H, Shim J, Kim H, Kong L, Meng Y, Wang K, Kim C and Kim J 2019 Path towards graphene commercialization from lab to market *Nature Nanotechnology* **14** 927.
2. Yin X, Tang C S, Wu D, Kong W, Li C, Wang Q, Cao L, Yang M, Chang Y-H, Qi D, Ouyang F, Pennycook S J, Feng Y P, Breese M B H, Wang S J, Zhang W, Rusydi A and Wee A T S 2019 Unraveling high-yield phase-transition dynamics in transition metal dichalcogenides on metallic substrates *Advanced Science* **6** 1802093.
3. Liu Y, Gao Y, Zhang S, He J, Yu J and Liu Z 2019 Valleytronics in transition metal dichalcogenides materials *Nano Research* **12** 2695.
4. Cui Y, Xin R, Yu Z, Pan Y, Ong Z Y, Wei X, Wang J, Nan H, Ni Z, Wu Y, Chen T, Shi Y, Wang B, Zhang G, Zhang Y W and Wang X 2015 High-performance monolayer ws_2 field-effect transistors on high-kappa dielectrics *Advanced Materials* **27** 5230.
5. Tan H, Fan Y, Zhou Y, Chen Q, Xu W and Warner J H 2016 Ultrathin 2D photodetectors utilizing chemical vapor deposition grown WS_2 with graphene electrodes *ACS Nano* **10** 7866.
6. Bernardi M, Palumbo M and Grossman J C 2013 Extraordinary sunlight absorption and one nanometer thick photovoltaics using two-dimensional monolayer materials *Nano Letters* **13** 3664.
7. Wang F, Kinloch I A, Wolverson D, Tenne R, Zak A, O'Connell E, Bangert U and Young R J 2017 Strain-induced phonon shifts in tungsten disulfide nanoplatelets and nanotubes *2D Materials* **4** 015007.
8. Gutierrez H R, Perea-Lopez N, Elias A L, Berkdemir A, Wang B, Lv R, Lopez-Urias F, Crespi V H, Terrones H and Terrones M 2013 Extraordinary room-temperature photoluminescence in triangular WS_2 monolayers *Nano Letters* **13** 3447.
9. Blundo E, Felici M, Yildirim T, Pettinari G, Tedeschi D, Miriametro A, Liu B, Ma W, Lu Y and Polimeni A 2020 Evidence of the direct-to-indirect band gap transition in strained two-dimensional WS_2 , MoS_2 and WSe_2 . *Physical Review Research* **2** 012024.
10. Eksik O, Gao J, Shojaee S A, Thomas A, Chow P, Bartolucci S F, Lucca D A and Koratkar N 2014 Epoxy nanocomposites with two-dimensional transition metal dichalcogenide additives *ACS Nano* **8** 5282.
11. Kim S K, Wie J J, Mahmood Q and Park H S 2014 Anomalous nanoinclusion effects of 2D MoS_2 and WS_2 nanosheets on the mechanical stiffness of polymer nanocomposites *Nanoscale* **6** 7430.
12. Vega-Mayoral V, Backes C, Hanlon D, Khan U, Gholamvand Z, O'Brien M, Duesberg G S, Gadermaier C and Coleman J N 2016 Photoluminescence from liquid-exfoliated ws_2 monomers in poly(vinyl alcohol) polymer composites *Advanced Functional Materials* **26** 1028.
13. Liu K, Yan Q, Chen M, Fan W, Sun Y, Suh J, Fu D, Lee S, Zhou J, Tongay S, Ji J, Neaton J B and Wu J 2014 Elastic properties of chemical-vapor-deposited monolayer MoS_2 , WS_2 , and their bilayer heterostructures *Nano Letters* **14** 5097.

14. Gong L, Young R J, Kinloch I A, Riaz I, Jalil R and Novoselov K S 2012 Optimizing the reinforcement of polymer-based nanocomposites by graphene *ACS Nano* **6** 2086.
15. Ahmadi M, Zabihi O, Jeon S, Yoonessi M, Dasari A, Ramakrishna S and Naebe M 2020 2D transition metal dichalcogenide nanomaterials: Advances, opportunities, and challenges in multi-functional polymer nanocomposites *Journal of Materials Chemistry A* **8** 845.
16. Gong L, Kinloch I A, Young R J, Riaz I, Jalil R and Novoselov K S 2010 Interfacial stress transfer in a graphene monolayer nanocomposite *Advanced Materials* **22** 2694.
17. Li Z, Young R J and Kinloch I A 2013 Interfacial stress transfer in graphene oxide nanocomposites *ACS Applied Materials & Interfaces* **5** 456.
18. Dadgar A M, Scullion D, Kang K, Esposito D, Yang E H, Herman I P, Pimenta M A, Santos E J G and Pasupathy A N 2018 Strain engineering and Raman spectroscopy of monolayer transition metal dichalcogenides *Chemistry of Materials* **30** 5148.
19. He X, Li H, Zhu Z, Dai Z, Yang Y, Yang P, Zhang Q, Li P, Schwingenschlogl U and Zhang X 2016 Strain engineering in monolayer WS₂, MoS₂, and the WS₂/MoS₂ heterostructure *Applied Physics Letters* **109** 173105.
20. Liu Z, Amani M, Najmaei S, Xu Q, Zou X, Zhou W, Yu T, Qiu C, Birdwell A G, Crowne F J, Vajtai R, Yakobson B I, Xia Z, Dubey M, Ajayan P M and Lou J 2014 Strain and structure heterogeneity in MoS₂ atomic layers grown by chemical vapour deposition *Nature Communications* **5** 5246.
21. Tweedie M E P, Sheng Y, Sarwat S G, Xu W, Bhaskaran H and Warner J H 2018 Inhomogeneous strain release during bending of WS₂ on flexible substrates *ACS Applied Materials & Interfaces* **10** 39177.
22. Tyurnina A V, Bandurin D A, Khestanova E, Kravets V G, Koperski M, Guinea F, Grigorenko A N, Geim A K and Grigorieva I V 2019 Strained bubbles in van der waals heterostructures as local emitters of photoluminescence with adjustable wavelength *ACS Photonics* **6** 516.
23. Zhao W, Ghorannevis Z, Chu L, Toh M, Kloc C, Tan P H and Eda G 2013 Evolution of electronic structure in atomically thin sheets of WS₂ and WSe₂ *ACS Nano* **7** 791.
24. MicroChem. Su-8 2000 permanent epoxy negative photoresist. http://www.microchem.com/pdf/SU-82000DataSheet2000_5thru2015Ver4.pdf.
25. Radisavljevic B, Radenovic A, Brivio J, Giacometti V and Kis A 2011 Single-layer MoS₂ transistors *Nature Nanotechnology* **6** 147.
26. Bissett M A, Worrall S D, Kinloch I A and Dryfe R A W 2016 Comparison of two-dimensional transition metal dichalcogenides for electrochemical supercapacitors *Electrochimica Acta* **201** 30.
27. Worsley M A, Shin S J, Merrill M D, Lenhardt J, Nelson A J, Woo L Y, Gash A E, Baumann T F and Orme C A 2015 Ultralow density, monolithic WS₂, MoS₂, and MoS₂/graphene aerogels *ACS Nano* **9** 4698.
28. Coleman J N, Lotya M, O'Neill A, Bergin S D, King P J, Khan U, Young K, Gaucher A, De S, Smith R J, Shvets I V, Arora S K, Stanton G, Kim H Y, Lee K, Kim G T, Duesberg G S, Hallam T, Boland J J, Wang J J, Donegan J F, Grunlan J C, Moriarty G, Shmeliov A, Nicholls R J, Perkins J M, Grieveson E M, Theuwissen K, McComb D W, Nellist P D and Nicolosi V 2011 Two-dimensional nanosheets produced by liquid exfoliation of layered materials *Science* **331** 568.
29. Li Z, Young R J, Wilson N R, Kinloch I A, Vallés C and Li Z 2016 Effect of the orientation of graphene-based nanoplatelets upon the Young's modulus of nanocomposites *Composites Science and Technology* **123** 125.
30. Mitioglu A A, Plochocka P, Jadcak J N, Escoffier W, Rikken G L J A, Kulyuk L and Maude D K 2013 Optical manipulation of the exciton charge state in single-layer tungsten disulfide *Physical Review B* **88** 245403.
31. Peimyoo N, Yang W, Shang J, Shen X, Wang Y and Yu T 2014 Chemically driven tunable light emission of charged and neutral excitons in monolayer WS₂ *ACS Nano* **8** 11320.
32. Park J, Lee W, Choi T, Hwang S H, Myoung J M, Jung J H, Kim S H and Kim H 2015 Layer-modulated synthesis of uniform tungsten disulfide nanosheet using gas-phase precursors *Nanoscale* **7** 1308.
33. Neumann C, Reichardt S, Venezuela P, Drogeler M, Banszerus L, Schmitz M, Watanabe K, Taniguchi T, Mauri F, Beschoten B, Rotkin S V and Stampfer C 2015 Raman spectroscopy as probe of nanometre-scale strain variations in graphene *Nature Communications* **6** 8429.
34. Li Z, Kinloch I A, Young R J, Novoselov K S, Anagnostopoulos G, Parthenios J, Galiotis C, Papagelis K, Lu C-Y and Britnell L 2015 Deformation of wrinkled graphene *ACS Nano* **9** 3917.
35. Wang Y, Cong C, Yang W, Shang J, Peimyoo N, Chen Y, Kang J, Wang J, Huang W and Yu T 2015 Strain-induced direct-indirect bandgap transition and phonon modulation in monolayer WS₂ *Nano Research* **8** 2562.
36. Kumar A and Ahluwalia P K 2012 Electronic structure of transition metal dichalcogenides monolayers 1h-MX₂ (M = Mo, W; X = S, Se, Te) from ab-initio theory: New direct band gap semiconductors *The European Physical Journal B* **85** 186.
37. Zhu Z Y, Cheng Y C and Schwingenschlöggl U 2011 Giant spin-orbit-induced spin splitting in two-dimensional transition-metal dichalcogenide semiconductors *Physical Review B* **84** 153402.
38. He K, Poole C, Mak K F and Shan J 2013 Experimental demonstration of continuous electronic structure tuning via strain in atomically thin MoS₂ *Nano Letters* **13** 2931.
39. Conley H J, Wang B, Ziegler J I, Haglund R F, Jr., Pantelides S T and Bolotin K I 2013 Bandgap engineering of strained monolayer and bilayer MoS₂ *Nano Letters* **13** 3626.
40. Chang C-H, Fan X, Lin S-H and Kuo J-L 2013 Orbital analysis of electronic structure and phonon dispersion in MoS₂, MoSe₂, WS₂, and WSe₂ monolayers under strain *Physical Review B* **88** 195420.
41. Li Z, Lv Y, Ren L, Li J, Kong L, Zeng Y, Tao Q, Wu R, Ma H, Zhao B, Wang D, Dang W, Chen K, Liao L, Duan X, Duan X and Liu Y 2020 Efficient strain modulation of 2D

- materials via polymer encapsulation *Nature Communications* **11** 1151.
42. Young R J, Gong L, Kinloch I A, Riaz I, Jalil R and Novoselov K S 2011 Strain mapping in a graphene monolayer nanocomposite *ACS Nano* **5** 3079.
43. Manikas A C, Pastore Carbone M G, Woods C R, Wang Y, Souli I, Anagnostopoulos G, Hadjinicolaou M, Novoselov K S and Galiotis C 2019 Stress transfer at the nanoscale on graphene ribbons of regular geometry *Nanoscale* **11** 14354.
44. Colangelo F, Morandi A, Forti S, Fabbri F, Coletti C, Di Girolamo F V, Di Lieto A, Tonelli M, Tredicucci A, Pitanti A and Roddaro S 2019 Local tuning of WS₂ photoluminescence using polymeric micro-actuators in a monolithic van der Waals heterostructure *Applied Physics Letters* **115** 183101.
45. Li Z, Kinloch I A and Young R J 2016 The role of interlayer adhesion in graphene oxide upon its reinforcement of nanocomposites *Philosophical Transactions of the Royal Society A: Mathematical, Physical and Engineering Sciences* **374** 20150283.
46. Young R J and Lovell P A, *Introduction to polymers*. CRC Press: Boca Baton, 2011.
47. Jiang T, Huang R and Zhu Y 2014 Interfacial sliding and buckling of monolayer graphene on a stretchable substrate *Advanced Functional Materials* **24** 396.
48. Carrascoso F, Li H, Frisenda R and Castellanos-Gomez A 2020 Strain engineering in single-, bi- and tri-layer MoS₂, MoSe₂, WS₂ and WSe₂ *Nano Research* Accepted.
49. Zhang Q, Chang Z, Xu G, Wang Z, Zhang Y, Xu Z-Q, Chen S, Bao Q, Liu J Z, Mai Y-W, Duan W, Fuhrer M S and Zheng C 2016 Strain relaxation of monolayer WS₂ on plastic substrate *Advanced Functional Materials* **26** 8707.
50. Mennel L, Paur M and Mueller T 2019 Second harmonic generation in strained transition metal dichalcogenide monolayers: MoS₂, MoSe₂, WS₂, and WSe₂ *APL Photonics* **4** 034404.
51. Mlack J T, Masih Das P, Danda G, Chou Y C, Naylor C H, Lin Z, Lopez N P, Zhang T, Terrones M, Johnson A T and Drndic M 2017 Transfer of monolayer TMD WS₂ and raman study of substrate effects *Scientific Reports* **7** 43037.
52. Berkdemir A, Gutiérrez H R, Botello-Méndez A R, Perea-López N, Elías A L, Chia C-I, Wang B, Crespi V H, López-Urías F, Charlier J-C, Terrones H and Terrones M 2013 Identification of individual and few layers of WS₂ using raman spectroscopy *Sci Rep* **3** 1755.
53. Li Z, Young R J, Papageorgiou D G, Kinloch I A, Zhao X, Yang C and Hao S 2019 Interfacial stress transfer in strain engineered wrinkled and folded graphene *2D Materials* **6** 045026.
54. Shah D U and Schubel P J 2010 Evaluation of cure shrinkage measurement techniques for thermosetting resins *Polymer Testing* **29** 629.
55. Zhao X, Papageorgiou D G, Zhu L, Ding F and Young R J 2019 The strength of mechanically-exfoliated monolayer graphene deformed on a rigid polymer substrate *Nanoscale* **11** 14339.
56. Hirunpinyopas W, Iamprasertkun P, Bissett M A and Dryfe R A W 2020 Tunable charge/size selective ion sieving with ultrahigh water permeance through laminar graphene membranes *Carbon* **156** 119.
57. Bicca S, Boland C S, O'Driscoll D P, Harvey A, Gabbett C, O'Suilleabhain D R, Griffin A J, Li Z, Young R J and Coleman J N 2019 Negative gauge factor piezoresistive composites based on polymers filled with MoS₂ nanosheets *ACS Nano* **13** 6845.
58. Papageorgiou D G, Li Z, Liu M, Kinloch I A and Young R J 2020 Mechanisms of mechanical reinforcement by graphene and carbon nanotubes in polymer nanocomposites *Nanoscale* **12** 2228.
59. Li Z, Slater T J A, Ma X, Yu Y, Young R J and Burnett T L 2019 The taxonomy of graphite nanoplatelets and the influence of nanocomposite processing *Carbon* **142** 99.
60. Wang W, Li Z, Prestat E, Hashimoto T, Guan J, Kim K S, Kingston C T, Simard B and Young R J 2020 Reinforcement of polymer-based nanocomposites by thermally conductive and electrically insulating boron nitride nanotubes *ACS Applied Nano Materials* **3** 364.
61. Zhou K, Jiang S, Bao C, Song L, Wang B, Tang G, Hu Y and Gui Z 2012 Preparation of poly(vinyl alcohol) nanocomposites with molybdenum disulfide (MoS₂): Structural characteristics and markedly enhanced properties *RSC Advances* **2** 11695.
62. Chou T-W, *Microstructural design of fiber composites*. Cambridge University Press: Cambridge, 1992.
63. Krenchel H, *Fibre reinforcement*. Akademisk Forlag: Copenhagen, 1964.
64. Young R J, Liu M, Kinloch I A, Li S, Zhao X, Vallés C and Papageorgiou D G 2018 The mechanics of reinforcement of polymers by graphene nanoplatelets *Composites Science and Technology* **154** 110.